Int. J. Heat Mass Transfer. Vol. 29, No. 7, pp. 1007–1019, 1986
Printed in Great Britain

0017–9310/86 $3.00 + 0.00
Pergamon Journals Ltd.

Melting in a horizontal tube with the solid either constrained or free to fall under gravity

E. M. SPARROW and G. T. GEIGER
Department of Mechanical Engineering, University of Minnesota, Minneapolis, MN 55455, U.S.A.

(*Received* 19 *November* 1985 *and in final form* 28 *January* 1986)

Abstract—Experiments and supplementary numerical solutions have been performed to study the melting of a solid encapsulated in a horizontal tube. In one set of experiments, the solid was constrained not to move, while in a second set of experiments the solid was able to fall freely under gravity. In the latter (i.e. unconstrained) case, the lower portion of the solid was separated from the tube wall by a narrow, liquid-filled gap. The numerical solutions enabled the rates of melting at the lower and upper portions of the unconstrained solid to be determined. At a given duration of the melting period, the amount of mass melted in the unconstrained mode exceeded that melted in the constrained mode by 50–100%, with a similar gain in energy transfer. For the unconstrained mode, about 90% of the melting occurred at the lower portion of the solid. Photographic evidence demonstrated that the melting process in the constrained mode is intrinsically three-dimensional, while in the absence of end effects the unconstrained-mode melting is two-dimensional.

INTRODUCTION

MELTING of a solid contained in a horizontal tube has evoked considerable current interest, as evidenced by the recent publication of several experimental and analytical studies, of which refs. [1–7] are representative. This interest has been motivated primarily by the use of solid–liquid phase change for the storage of thermal energy. In these investigations, consideration was given either to a melting solid which is constrained to prevent its possible movement due to gravity [1–5] or to a solid which is free to fall under gravity [6, 7]. In the first case, the melting solid is completely surrounded by the liquid melt and the energy needed for the melting is transported from the tube wall to the solid–liquid interface by natural convection in the liquid.

In the second case, the solid is pressed by gravity against the lower portion of the tube wall. However, touching contact between the lower portion of the solid and the wall is not achieved. Rather, owing to the continuous production of liquid by the melting solid, a thin, liquid-filled gap necessarily exists between the solid and the wall. The liquid produced by the melting is continuously squeezed out of the gap by the force which presses the solid against the wall. The energy needed for the melting of the solid which borders the gap is transported by conduction across the gap. On the other hand, the melting of the upper portion of the solid is controlled by natural convection in the liquid melt which occupies the space between the solid and the upper portion of the tube wall.

The two aforementioned modes of melting will be encountered frequently during the present paper and it will be convenient to assign brief, descriptive designations to them. The case of the constrained solid will be designated as the centered mode, while the case where the solid is pressed against the tube will be referred to as the wall-adjacent mode.

Despite the available literature on melting in a horizontal tube, there are a number of key issues which remain unresolved. Among these, perhaps the issue of greatest practical importance is the relative magnitudes of the melting rates in the centered and wall-adjacent modes. This assessment can be made with the highest degree of certainty if experiments on the two modes were to be conducted using the same apparatus, with everything else being identical. It appears that the same apparatus was used in refs. [4, 7], although ref. [7], the more recent of the two papers, makes no mention of this. Furthermore, different types of results are presented in these two works, virtually ruling out a comparison between the centered and wall-adjacent modes.

Another key issue that remains unresolved is whether the melting process is two- or three-dimensional (i.e. absence or presence of axial variations). In the available analytical work on the problem, it has been standard to assume that the process is two-dimensional. In the experimental work, the common practice has been to use tubes with relatively small length-to-diameter ratios, e.g. 1.25 [4, 7] and 1.56 [5], which tends to exaggerate the role of hydrodynamic end effects and also, perhaps, of thermal end effects. The melting rates reported in refs. [4, 5, 7] were obtained from optical methods under the assumption that axial variations were absent.

A third issue, which is pertinent only to the wall-adjacent mode, is the relative rates of melting at the lower and upper portions of the solid, respectively controlled by conduction across the thin, liquid-filled gap and by natural convection in the pool of liquid melt. This issue was not addressed in the analysis of ref. [7]. Even if it had been examined there, con-

NOMENCLATURE

A surface area
c specific heat of liquid
c_{sol} specific heat of solid
E_{max} maximum value of E_{tot}
E_s sensible energy input to liquid
E_{tot} sum of E_λ and E_s
E_λ energy to melt mass M
$E_{\lambda,max}$ energy to melt mass M_{tot}
Fo Fourier number, $\alpha t/R^2$
g force of gravity
k thermal conductivity of liquid
L length of tube
M melted mass
M_{tot} total mass available for melting
$\dot{M}$ rate of melting
N number of cells
Nu local Nusselt number, $[q/(T_w - T^*)]R/k$
p pressure
Q surface-integrated rate of heat transfer
q local rate of heat transfer per unit area
R radius of tube
Ra Rayleigh number, $g\beta(T_w - T^*)R^3/\alpha\nu$
r radial coordinate
S_c subcooling parameter, equation (22)
Ste Stefan number, $c(T_w - T^*)/\lambda$
$(Ste)^*$ corrected Ste for subcooling of solid
T temperature
T_b liquid bulk temperature
T_w water bath temperature
T^* melting temperature
t time
u velocity in r-direction
V mean velocity at mouth of gap
v velocity in θ-direction
w average gap thickness.

Greek symbols
α thermal diffusivity of liquid
β thermal expansion coefficient
θ angular coordinate, Fig. 1
λ latent heat of melting
μ viscosity of liquid
ν kinematic viscosity of liquid
ρ density of liquid.

Subscripts
lower on lower surface of solid
upper on upper surface of solid.

siderable uncertainty would have occurred in the upper-surface melting rates since the natural convection was treated in an oversimplified manner (the source of the assumed heat transfer coefficient is not cited).

The foregoing discussion sets the stage for the present investigation, which includes both experimental and numerical work. Experiments utilizing the same apparatus were performed for both the centered and wall-adjacent modes of melting. These experiments were carried out over a wide range of melting period durations (described in dimensionless terms by the product of the Fourier and Stefan numbers) and for four values of the difference between the tube wall temperature and the melting temperature (~Stefan number). A length-to-diameter ratio of the containment tube equal to 5 was used in conjunction with foam insulation to minimize end effects. The phase-change medium was 99% pure n-eicosane paraffin with a melting temperature of 36.3°C. The results of these experiments yielded a definitive comparison of the two modes of melting. Also, the results for the individual modes are compared with the relevant literature.

The issue of the axial uniformity or nonuniformity of the melting process (i.e. two- or three-dimensionality) was also investigated experimentally, with the key results being obtained from photographs of the residual solid which remained at the end of the melting period.

The subdivision of the total amount of melting between the upper and lower surfaces in the wall-adjacent mode was determined from finite-different solutions for natural convection in the odd-shaped region between the upper surfaces of the melting solid and the tube wall.

EXPERIMENTS

Apparatus

The containment tube within which the melting occurred consisted of a cylindrical brass sleeve with insulating end caps. The internal dimensions of the tube were 3.810 × 19.05 cm (diameter × length), yielding an aspect ratio of 5. Brass was used for the tube body because of its relatively high thermal conductivity and easy machinability (the sleeve was fabricated by boring a solid rod). The bore of the sleeve was polished and lapped to a mirror finish, while its external surface was turned to yield a 0.318 cm wall thickness. Copper was considered for the sleeve but was rejected because of its less favorable machining characteristics, while aluminum reacts electrochemically with water and was, therefore, unsuitable since the tube was immersed in a water bath during the experiment.

Each end cap consisted of a section of Delrin plastic rod that had been hollowed out to create an insulation cavity. The cavity was filled with a 2.54-cm-thick cylindrical block of closed-pore polystyrene (Styrofoam). With the insulation in place, the cavity was

sealed with a thin Delrin disk, which also served as the face of the end cap which contacted the paraffin.

For the experiments on melting in the centered mode, one of the end caps was modified to fix the solid and prevent its fall to the bottom of the tube. Specifically, the thin Delrin disk which closed the insulation cavity was fitted with a finger-like Delrin rod, 0.635 cm in diameter and 3.81 cm long, which extended axially into the tube bore. The rod was threaded to facilitate the adhesion of the solid paraffin to it.

To support the tube so that its axis would be horizontal, a brass shaft was attached perpendicular to the outside surface of the brass sleeve, midway between the ends. With the tube horizontal, the shaft pointed vertically upward. The attachment of the shaft to the tube was facilitated by a raised boss which had been left on the sleeve during its fabrication.

The shaft served not only to support the tube but also as a reservoir to receive the excess volume of the liquid melt which is created by the density decreases which accompany the melting and the subsequent temperature increase of the liquid. For this purpose, the shaft was hollowed out. At the top of the shaft, the hollowed-out space was vented to the atmosphere to facilitate the escape of the air displaced from the space by the incoming liquid melt.

Two constant-temperature water baths were used during each melting experiment. Prior to the melting period, one of the baths was employed to bring the tube and the encapsulated solid paraffin to a uniform temperature just below the 36.3°C melting temperature of the paraffin. The second bath served as the thermal environment for the tube during the melting period. It consisted of a large, well-insulated stainless-steel tank filled with water. The water was highly agitated to achieve a large value of the heat transfer coefficient at the external surface of the containment tube. An immersed temperature controller maintained temperature constancy to within 0.1°C (verified by an ASTM-certified thermometer). A strut which overhung the tank was provided for the attachment of the support shaft of the containment tube.

The key quantities measured during the course of the experiments were the masses of the solid at the beginning and end of the melting period, the temperatures of the thermal equilibration and melting environment baths, and the temperature of the liquid at the end of the melting period. These measurements were supplemented by photographs of the solid remaining at the end of the melting period. The mass measurements were made with a triple-beam balance having a capacity of 2610 g and a resolution of 0.1 g, while the bath temperatures were sensed by the aforementioned certified thermometers.

A special guarded calorimeter was used for the measurement of the liquid bulk temperature. It consisted of a double-walled, open-topped Styrofoam container whose base was cemented to the bottom of a larger plastic container which was also open-topped. The annular space between the containers was filled with water whose temperature closely approximated that of the liquid paraffin, which was situated in the Styrofoam container. A nylon rod equipped with two thermocouples was used to stir the paraffin. The procedure followed in the bulk temperature measurement will be described shortly.

Experimental procedure

For a given thermal operating condition defined by the temperature of the melting environment bath and the melting temperature of the solid, the timewise increase of the melted mass was measured in a succession of independent data runs. The preparations for each data run were begun with the containment tube empty and with all traces of the paraffin from the preceding run eliminated. To begin, one of the end caps was put in place, either the finger-equipped cap for the centered-mode melting experiments or the flat-faced cap for the wall-adjacent-mode experiments. Then, the tube was positioned vertically with its open (i.e. uncapped) end facing upward in preparation for the introduction of liquid paraffin. A sleeve-like extension was then affixed to the open end of the tube to facilitate the filling operation.

The tube was filled with liquid paraffin to a height about half way up the extension piece, after which it was placed in an ice bath. Void formation during the freezing of the paraffin was prevented by irradiation of its exposed upper surface by a heat lamp set at low intensity. After completion of solidification, the upper surface of the paraffin was made flat by contact with a heated metal disk whose controlled depth of penetration into the extension piece also fixed the length of the solid specimen. Once these operations were completed, the extension piece was removed and the end cap put in place, after which the tube and its contents were weighed.

The specimen length for the centered-mode melting experiments was made exactly equal to the distance between the end caps, when both caps were in place in the tube. However, for the wall-adjacent-mode experiments, the specimens were made about 0.16 cm shorter (0.08 cm at each end) than the intercap distance. This practice was adopted to avoid tight contact between the solid and the end caps, since such contact would prevent the free fall of the solid during the melting period. The actual clearance which prevailed at the initiation of melting was less than the aforementioned 0.16 cm due to the expansion of the solid during the equilibration period.

The tube and its charge of solid paraffin were placed in the equilibration bath for a period of at least 6–7 h. During this time, the temperature of the melting environment bath was brought to the desired value. To initiate the melting period, the tube was transferred from the equilibration bath to the melting environment bath, a process which was accomplished in about 10 s.

To terminate the melting, the tube was taken from the environment bath, and one of the end caps was removed. The unmelted solid was immediately extracted from the tube and, without delay, the liquid melt was poured into the calorimeter, whose water buffer had previously been readied. The stirring rod was used to mix the liquid and during this time the outputs of the thermocouples attached to the rod were read and recorded by a pre-programmed datalogger. The stirring was continued until the temperature attained a steady, uniform value, which usually required about 10 s. Attention was then turned to the extracted solid, which was wiped free of any adhering liquid and then weighed. Representative extracted solid specimens were photographed to document differences in the centered and wall-adjacent modes of melting.

Data reduction

The melting results will be reported in terms of the amount of mass liquefied between the onset of melting ($t = 0$) and any subsequent time t. This quantity, to be denoted by M, was determined from mass measurements made before and after the melting period. For a dimensionless presentation, M will be ratioed with the total amount of mass M_{tot} in the containment tube that is available for melting.

If E_λ is the energy which is absorbed at the solid–liquid interface to liquify the mass M, then

$$E_\lambda = \lambda M \tag{1}$$

where λ is the latent heat of melting. Also, since $E_{\lambda,max} = \lambda M_{tot}$, it follows that $E_\lambda/E_{\lambda,max} = M/M_{tot}$. Energy is also supplied to the liquid melt to bring its temperature from T^* to some higher value. If T_b denotes the liquid bulk temperature at a time t when the melted mass is M, then the sensible energy E_s absorbed by the liquid melt between $t = 0$ and $t = t$ is

$$E_s = M\bar{c}(T_b - T^*) \tag{2}$$

where

$$\bar{c} = \left[\int_{T^*}^{T_b} c\,dT\right] \Big/ (T_b - T^*). \tag{3}$$

Since the specific heat c can be represented as a linear function of temperature for n-eicosane paraffin [8], $\bar{c}$ corresponds to $(T_b + T^*)/2$.

The total energy E_{tot} transferred from the tube wall to the encapsulated phase-change medium between $t = 0$ and $t = t$ is the sum of E_λ and E_s, so that

$$E_{tot} = M[\lambda + \bar{c}(T_b - T^*)]. \tag{4}$$

The maximum value of E_{tot}, denoted by E_{max}, occurs when all the solid has melted and the liquid has attained the temperature T_w, that is

$$E_{max} = M_{tot}[\lambda + \bar{c}(T_w - T^*)] \tag{5}$$

where $\bar{c}$ now corresponds to $(T_w + T^*)/2$. The energy transfer results will be presented both in terms of E_{tot}/E_{max} and E_s/E_λ.

The duration t of the melting period will be represented in dimensionless terms as the *FoSte* product, where the Fourier number *Fo* and the Stefan number *Ste* are defined as

$$Fo = \alpha t/R^2, \quad Ste = c(T_w - T^*)/\lambda \tag{6}$$

in which R is the radius of the tube bore. The Stefan number also serves as a dimensionless representation of the bath-to-melting temperature difference $(T_w - T^*)$. Another dimensionless group used in the presentation of results is the Rayleigh number

$$Ra = g\beta(T_w - T^*)R^3/\alpha\nu. \tag{7}$$

The temperature used for the evaluation of the thermophysical properties of the liquid that appear in equations (6) and (7) will be noted when the results are presented.

NUMERICAL SOLUTIONS

As noted in the Introduction, one of the objectives of the present work is to determine the individual contributions of the melting at the lower and upper surfaces of the solid to the overall melted mass M for the wall-adjacent mode. The melting at the lower surface is controlled by conduction across a thin, liquid-filled gap, while that at the upper surface is controlled by natural convection in a relatively larger pool of liquid. The approach to be used here is to obtain numerical solutions for the natural convection problem, use this information to compute the melting at the upper surface, and then compare this quantity with the overall melted mass that was measured in the experiments.

Computational model and boundary conditions

To facilitate the description of the analysis, reference may be made to Fig. 1, which is a schematic diagram of the tube cross section at a representative time t. As seen there, the solid is lens-shaped and is situated at the bottom of the tube, with a narrow gap between the solid and the tube wall. The lens shape

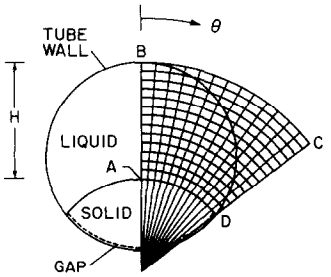

FIG. 1. Schematic diagram of the tube cross section and superposed finite-difference grid.

portrayed in the figure is a true representation of the cross section of the solid, as witnessed by observations made during the experimental portion of the work. These observations were facilitated by sectioning the solid at several axial locations after its withdrawal from the tube at the end of the melting period. The outlines of the cross sections thus exposed were traced on paper to provide a permanent record.

The aforementioned experimental observations yielded two highly relevant facts: (1) there were no axial variations of the thickness or shape of the solid for the wall-adjacent melting mode; and (2) the radius of the upper surface of the solid was equal to that of the tube radius, within measurement accuracy. Note that the latter finding is in accord with those of ref. [7], while the former suggests that the problem can be treated on a two-dimensional basis.

During the melting process the solid–liquid interface recedes, so that the size of the liquid-filled space above the upper surface of the solid increases with time. However, the change in the size of the space is slow compared with the capability of the natural convection to accommodate the change. Therefore, the numerical analysis of the natural convection will be made on a quasi-steady basis. In particular, the steady-state natural convection problem will be solved for each of a succession of fixed-geometry, liquid-filled spaces, each defined by the pre-assigned height H of the cross-section symmetry line AB (see Fig. 1).

Owing to symmetry, only half the liquid space need be considered for the numerical analysis. In Fig. 1, the half space is bounded by ABDA. The segments BD and AD are both circular arcs of radius R, which suggests the use of (r, θ) polar coordinates. However, the origins from which the two arcs are drawn are different, so that BD and AD cannot both be coordinate lines in a single (r, θ) coordinate system. Since the heat transfer rate at the solid–liquid interface is of primary interest, and since AD coincides with the interface, it is natural to use a coordinate system in which AD is a coordinate line. Consequently, the origin of the coordinate system was chosen to coincide with the origin from which the arc AD is drawn (with radius R). Such a coordinate system is illustrated in Fig. 1.

Also illustrated in the figure is an array of control volumes used to implement the finite-difference work. To maintain clarity, a 13×13 array ($=169$) is shown, whereas the actual numerical work was performed with a 30×30 array ($=900$). Note that the arc BD does not lie along the control volume boundaries but, rather, it cuts through the control volumes—a logical outcome of the choice of the origin of coordinates.

In a situation like this, it is common to approximate the actual boundary (i.e. BD) by a stepped boundary in which the steps are the sides of the control volumes cut by the actual boundary. Fortunately, with a dense array of control volumes such as the 30×30 array used here, the stepped boundary is a good approximation of the actual boundary. The layout of the steps was performed systematically (rather than intuitively) as described in ref. [9].

The general purpose finite-difference algorithm [10] used here is not able to accommodate directly the stepped boundaries. Consequently, the solution domain was artificially extended so that its outer boundary would lie on a coordinate line and would, therefore, be free of steps. This extension resulted in a solution domain bounded by ABCDA in Fig. 1. The extended solution domain contains a number of control volumes which lie outside the actual domain. The procedure used to deactivate the additional control volumes will be described shortly, after the boundary conditions have been discussed.

With regard to the boundary conditions, it is necessary that they reflect the fact that there is a throughflow of liquid through the solution domain. The liquid enters the domain adjacent to point D, coming from the mouth of the gap which bounds the lower surface of the solid, and it exits via a port centered at point B. The rate of inflow will be provided to the computer program as an input, determined from the experimental data by a procedure soon to be outlined, while the rate of outflow was made equal to the rate of inflow.

Aside from the aforementioned exit port, the boundary conditions on the actual boundary BD of the solution domain are: (a) zero r and θ velocities; and (b) temperature $= T_w$. Note that the latter neglects the small temperature drop across the boundary layer external to the tube. In the numerical model, these boundary conditions were applied at the boundaries BC and CD of the extended solution domain. Furthermore, in all of the additional control volumes associated with the extended domain, the viscosity μ and the thermal conductivity k were set equal to infinity. These choices for μ and k automatically impose boundary conditions (a) and (b) on the stepped boundary approximation of BD.

At the exit port, the boundaries BC and BD are virtually coincident. At this part of the boundary, the velocity was constrained to be radial and the temperature was set equal to T_w. The velocity was adjusted to satisfy an overall mass balance, as noted earlier. On the symmetry line AB, the usual symmetry boundary conditions apply: (c) zero θ derivatives of the r velocity and the temperature; and (d) zero θ velocity.

Along the surface AD of the solid, aside from the inflow zone adjacent to point D, the zero velocity condition (a) applies, and the temperature $= T^*$ (melting temperature). It remains to determine the size of the inflow zone and the velocity of the inflowing fluid. To begin the determination, it will first be assumed that the gap which separates the lower surface of the solid from the tube wall is of uniform thickness w. It is further assumed that the heat transfer across the gap is by one-dimensional conduction. Then, if dM/dt denotes the rate of melting, it follows that

$$\lambda(dM/dt) = kA_{\text{lower}}(T_w - T^*)/w \qquad (8)$$

or

$$w = kA_{\text{lower}}(T_w - T^*)/\lambda(\mathrm{d}M/\mathrm{d}t) \quad (9)$$

where A_{lower} is the area of the lower surface of the solid which bounds the gap. A typical value of w computed from equation (9) is 0.04 cm.

The RHS of equation (8) is the heat transfer across the gap so that, strictly speaking, $\mathrm{d}M/\mathrm{d}t$ should correspond to the rate of melting at the surface which bounds the gap. However, only $\mathrm{d}M/\mathrm{d}t$ for the entire solid (both upper and lower surfaces) is available from the experimental data, so that that information will be used as input to equation (9). It will be seen later that this approach does not lead to significant errors. With w from equation (9), the mean velocity V at the mouth of the gap is

$$V = (\mathrm{d}M/\mathrm{d}t)/2\rho wL \quad (10)$$

where the 2 in the denominator reflects the fact that the gap has two mouths and L is the axial length of the solid.

Consideration was also given to the possibility that the gap thickness may vary circumferentially. Inspection of the paraffin samples from the experiments suggested that the gap thickness increased in the direction from the low point of the solid to the mouth. The simplest representation for such a change is that the thickness varies linearly, starting with zero thickness at the low point and culminating in a thickness at the mouth which is twice the average value given by equation (9). The velocity V at the double-thickness mouth is half of that given by equation (10).

Numerical solutions were carried out both for inflow zones of width w [equation (9)] and $2w$. As noted earlier, the inflow zone is situated adjacent to point D on arc AD (Fig. 1). The finite-difference grid was laid out so that two control volumes were developed circumferentially across the opening of the mouth of the gap. The velocity V at the mouth was resolved into r and θ velocity components. A linear temperature distribution was assumed to prevail across the mouth.

The actual grid deployment used in the computations will now be discussed. A common radial dimension was used for all control volumes. The circumferential dimension of the control volumes adjacent to the symmetry line AB was chosen to match the size of the exit port which is centered at point B. In turn, the exit port size for the computations was made equal to that of the experimental apparatus. The circumferential extent of the control volumes adjacent to the line CD was governed by the size of the gap mouth. Aside from the aforementioned control volumes adjacent to AB and CD, the circumferential dimensions of all the other control volumes were identical. As noted earlier, a grid composed of an array of 30×30 control volumes was used.

Governing equations

The governing differential equations which express the conservation laws were written in accordance with the quasi-steady model, excluding terms involving $\partial/\partial t$. The density differences which create the natural convection flow were represented by the Boussinesq approximation, but aside from this, all other properties were assumed to be constant. To achieve a compact presentation, the following notation will be used

$$\partial/\partial r = \partial_r, \quad \partial/\partial\theta = \partial_\theta, \quad \partial^2/\partial\theta^2 = \partial_\theta^2. \quad (11)$$

The radial velocity component will be denoted by u and the tangential velocity component by v.

The mass, r-momentum, θ-momentum and energy equations will now be written as they are needed for the general purpose computer program of [10]

$$\partial_r(ru) + \partial_\theta v = 0 \quad (12)$$

$$\rho[u\,\partial_r u + (v/r)\,\partial_\theta u] = -\partial_r p + (\mu/r)\,\partial_r(r\,\partial_r u) + (\mu/r^2)\,\partial_\theta^2 u + S_r \quad (13)$$

$$\rho[u\,\partial_r v + (v/r)\,\partial_\theta v] = -(1/r)\,\partial_\theta p + (\mu/r)\,\partial_r(r\,\partial_r v) + (\mu/r^2)\,\partial_\theta^2 v + S_\theta \quad (14)$$

$$\rho c_p[u\,\partial_r T + (v/r)\,\partial_\theta T] = (k/r)\,\partial_r(r\,\partial_r T) + (k/r^2)\,\partial_\theta^2 T. \quad (15)$$

All terms in the foregoing equations except the source terms S_r and S_θ are already reduced to finite-difference form in the computer program of ref. [10]. The source terms are

$$S_r = -\rho\beta g_r T + \rho v^2/r - \mu u/r^2 - (2\mu/r^2)\,\partial_\theta v \quad (16)$$

$$S_\theta = -\rho\beta g_\theta T - \rho uv/r - \mu v/r^2 + (2\mu/r^2)\,\partial_\theta u \quad (17)$$

in which g_r and g_θ are the r and θ components of the gravity vector. The components of the source terms were discretized by using a central difference approximation for derivatives and linearly interpolating the dependent variables at non-gridpoint locations.

The solutions of the finite-difference equations were obtained using the SIMPLE algorithm [10]. To improve the rate of convergence, the block correction procedure of ref. [11] was incorporated into the computer program.

Melting rates

Attention will now be turned to the application of the numerical solutions to the determination of the rate of melting at the upper surface of the solid. Let q_i denote the rate of heat transfer per unit area at position θ_i on the surface, where q_i was determined from the solutions by making use of the finite-difference form of Fourier's law. If q_i pertains to a control volume which subtends an angle $\Delta\theta_i$ on the upper surface of the solid, then the rate of heat transfer Q at the entire surface is

$$Q = 2\sum q_i R\Delta\theta_i L \quad (18)$$

where the sum extends over all the control volumes which contact the surface. The factor 2 appearing in equation (18) takes account of the symmetric portion of the upper surface which is not included in the sum.

The rate of melting at the upper surface then follows from equation (18) as

$$\dot{M}_{\text{upper}} = Q/\lambda. \tag{19}$$

Also, q_i can be used to evaluate a local Nusselt number from the defining equation

$$Nu = [q_i/(T_w - T^*)]R/k \tag{20}$$

The sensible energy stored in the liquid can be determined by evaluating the bulk temperature T_b from the finite-difference form of the integral definition

$$T_b = \left[\int T\,dA\right] \Big/ \left[\int dA\right]. \tag{21}$$

The integration extends over the control volumes within the original solution domain (excluding the additional control volumes of the extended solution domain). Once T_b is available, E_s follows from equation (2) and E_{tot} from equation (4).

PATTERNS OF MELTING

The description of the patterns of melting is facilitated by reference to the photographs displayed in Figs. 2 and 3. The first of these figures conveys representative end views of the melting solid, respectively for the centered mode in part (a) and the wall-adjacent mode in part (b). Figure 3 shows representative longitudinal views for both the centered mode [parts (a) and (b)] and the wall-adjacent mode [part (c)].

Centered mode

Attention will first be turned to the centered mode. In the end view [Fig. 2(a)], there are radial lines which emanate from a point situated in the upper part of the solid. Since this point coincides with the center of the tube, it is apparent that more melting occurs on the upper surface of the solid than on the lower surface. This is as expected, since natural convection delivers warmer fluid to the upper portion of the tube cross section and cooler fluid to the lower portion. Indeed, in each vertical half of the liquid melt, a general recirculation can be envisioned in which the liquid rises along the tube wall and descends along the solid.

It is also evident from Fig. 2(a) that the melting solid is by no means circular in cross section. In particular, the flattened sides of the lower part of the cross section suggest that there are fluid flows present other than the aforementioned general recirculation.

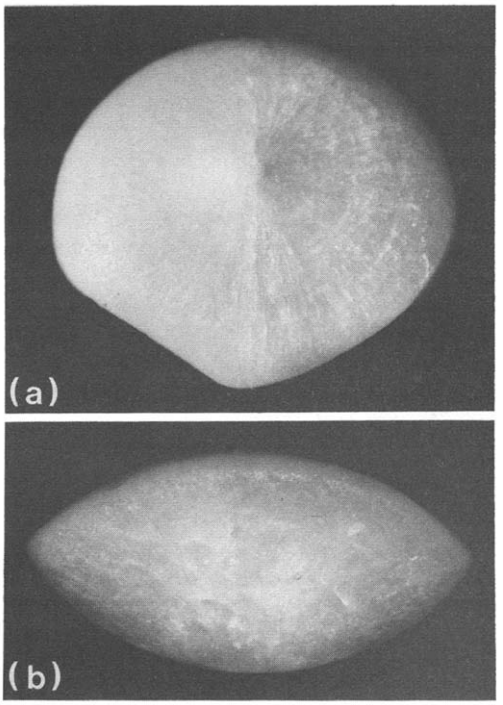

FIG. 2. End views of melting solid.

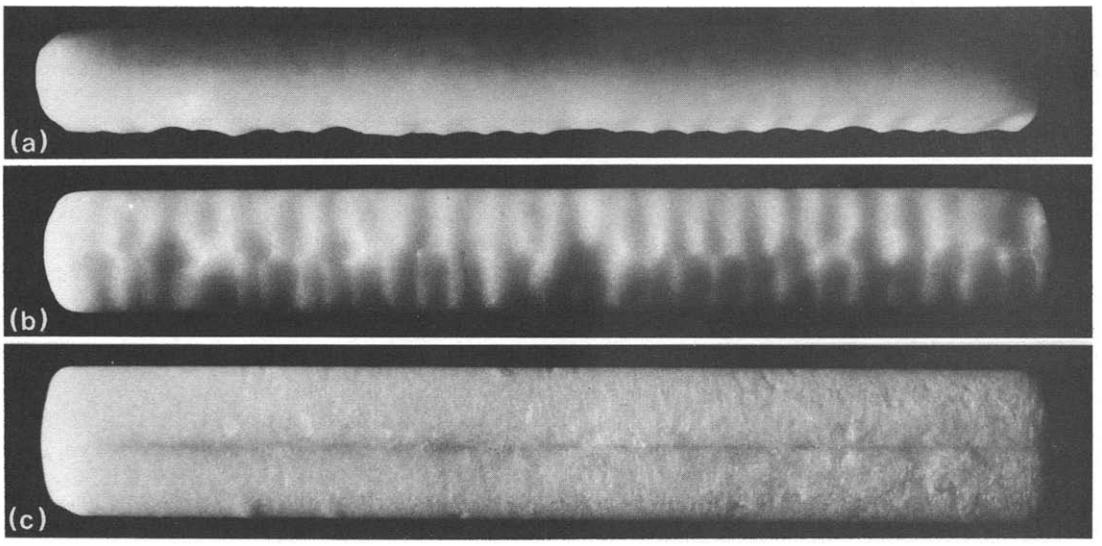

FIG. 3. Longitudinal views of the melting solid.

In this regard, it may be noted that the liquid melt situated between the lower portions of the tube and the solid is in a thermally unstable state since the temperature of the former ($\sim T_w$) exceeds that of the latter (T^*). It is well known that such an unstable state gives rise to cellular convection, which is generally three-dimensional.

To examine this issue, it is helpful to turn to Fig. 3(a), which is a longitudinal view of the melting solid of Fig. 2(a). The photograph shown in Fig. 3(a) was taken from the side, with the lower edge of the photo coinciding with the bottom of the solid and the upper edge of the photo coinciding with the top of the solid. As can be seen in the figure, the bottom of the solid is by no means smooth. Rather, it is characterized by nearly periodic undulations consisting of successive peaks and valleys. These undulations reflect the presence of a cellular, periodic, three-dimensional flow.

This three-dimensional flow affects the entire lower half of the solid, not just the very bottom, as witnessed by Fig. 3(b)—a longitudinal view looking upward at the solid from below. The alternating white and black bands respectively correspond to the aforementioned peaks and valleys [note that both Figs. 2(a) and 3(b) reflect a modest asymmetry at the lower sides of the solid, which is not unexpected in light of the thermal instability].

For given thermal operating conditions [i.e. given $(T_w - T^*)$], it was observed that the longer the duration of the melting period, the fewer the cells and the greater the axial extent of each cell. Also, since the distance between the solid and the tube wall increases with the duration of the melting period, the greater is the radial extent of the cells. Therefore, the aspect ratio of a cell (ratio of axial to radial dimensions) tends to remain constant, which is consistent with literature information for cellular convection.

The timewise variation of the number of cells N was determined for each thermal operating condition, and this information is presented in Fig. 4. On the ordinate, the number of cells is plotted per unit tube length L (normalized by the tube radius R), while the abscissa is the *FoSte* dimensionless time. The data are parameterized by the Stefan number *Ste*, which is the dimensionless counterpart of $(T_w - T^*)$. The thermophysical properties appearing in *Fo* and *Ste* were evaluated at the melting temperature T^*. As seen from the figure, the decrease of N with time is rapid at first but becomes increasingly more gradual as time proceeds. For the most part, the data are not very sensitive to *Ste*, nor is there a consistent ordering with *Ste*.

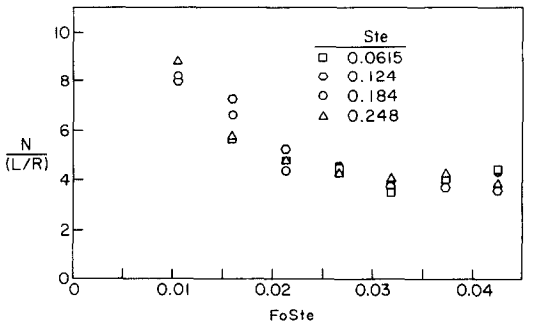

FIG. 4. Number of cells deployed along the length of the melting solid (centered mode of melting).

The existence of axial variations in the thickness of the melting solid [Figs. 3(a) and (b)] suggests that end-view-based photographic methods for determining the instantaneous mass of the solid be used with caution, especially for the centered mode. For instance, in refs. [4, 5], the mass was deduced by measuring the area of the solid from end-view photographs such as that of Fig. 2(a). However, looking lengthwise, such a photographic view sees only the highest points of the solid but not the low points. Therefore, such an approach tends to underestimate the amount of melted mass. For instance, for Fig. 2(a), there is about an 11% difference in the thickness of the solid between the high and low points. Another possible source of underestimation is that possible additional melting adjacent to the ends of the solid is not recognized by the photographic approach.

Three-dimensional motions in natural convection flow in horizontal annuli of fixed dimensions (i.e. without phase change) have been encountered in the published literature [12–14]. It would appear that the present flow pattern is akin to the three-dimensional spiral flow described in ref. [12]. However, the three-dimensional spiral flow patterns photographed in ref. [13] and more recently in ref. [15] included three-dimensional motions in the thermally stable portion of the annulus (i.e. the upper part of the annulus) as well as in the thermally unstable region. However, for the present situation, there was no indication of three-dimensionality in the stable region.

The issue of whether the present cellular pattern consisted of hexagonal cells or roll cells cannot be resolved with total certainty. However, from the results of refs. [16, 17] for convective instability between horizontal parallel plates, it appears that roll cells are more likely (see ref. [9] for a more complete discussion of this issue).

Wall-adjacent mode

The end-view photograph for the wall-adjacent mode, Fig. 2(b), displays the lens shape that was alluded to earlier. Both the upper and lower surfaces of the solid may be well represented by circular arcs of nearly equal radii. Furthermore, both surfaces are smooth and are uniform in the axial direction. In confirmation of this, a longitudinal view of the solid is presented in Fig. 3(c), with the photograph taken looking upward from below. The dark stripe which runs the length of the photo is at the original centerline of the solid and reflects the fact that that line was the last portion of the solid to freeze during the pre-run preparation of the test specimen.

All of the extracted solid samples for the wall-

adjacent mode of melting indicated that the fluid flow in the liquid melt was two-dimensional.

MELTED MASS

Comparisons of the modes of melting

The experimentally determined timewise variations of the melted mass for both the wall-adjacent and centered modes of melting are presented in Fig. 5. On the ordinate, the mass M melted between $t = 0$ and a later time $t = t$ is plotted as a ratio with the total mass M_{tot} in the tube that is available for melting. The abscissa is the dimensionless time *FoSte*, while the data are parameterized by *Ste*, which is the dimensionless counterpart of the overall temperature difference $(T_w - T^*)$. Again, the thermophysical properties of the liquid are evaluated at T^*.

An overview of Fig. 5 indicates that substantially greater amounts of melting occur in the wall-adjacent mode than in the centered mode—i.e. when the solid is free to fall to the bottom of the tube than when it is constrained. Depending on the value of *Ste*, the M values for the former mode may exceed those for the latter mode by 50–100%. This qualitative relationship between the two modes of melting is not unexpected, but the comparison conveyed by Fig. 5 is believed to be the first demonstration of the quantitative relationship between the modes. Clearly, to achieve rapid phase change, the melting solid should not be constrained.

The decisive difference between the two modes of melting lies in the difference in the mechanisms by which heat is transported from the tube wall to the solid–liquid interface. The centered mode depends on natural convection to convey the heat across a moderately thick liquid layer, while in the wall-adjacent mode the heat transfer is primarily accomplished by conduction across a narrow gap.

These different transfer mechanisms are reflected in the Stefan number dependences of the M/M_{tot} results, as can be seen in Fig. 5. In the wall-adjacent case, the dependence is weak, with M/M_{tot} decreasing very slightly with increasing *Ste* at a fixed value of *FoSte*. This behavior is exactly that encountered in classical Stefan melting, which is a pure conduction problem. The Stefan solution shows that at a fixed *FoSte*, M respectively decreases by about 1% and 4% for $Ste = 0.06$ and 0.25, relative to the M value at $Ste = 0$. This occurs because the larger sensible heat absorption in the liquid which is associated with larger *Ste* makes less heat available for the phase change.

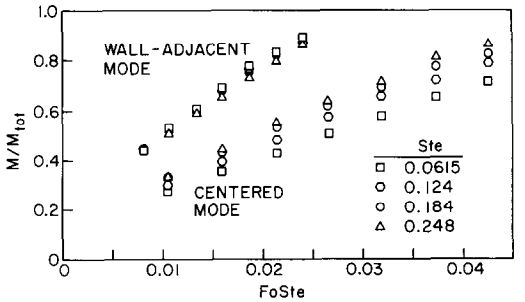

FIG. 5. Comparison of melting in the centered and wall-adjacent (i.e. constrained and unconstrained) modes.

In contrast to the foregoing, the M/M_{tot} values for the centered case are quite sensitive to *Ste* and increase as *Ste* increases. To rationalize this behavior, it should be noted that in this case, *Ste* serves much more as an index of the strength of the natural convection [i.e. $Ste \sim (T_w - T^*)$] than as a measure of the sensible heat absorption. Thus, as *Ste* increases, so does the vigor of the natural convection, with a corresponding increase in M/M_{tot}.

Comparison of each mode with the literature

The present results for each of the melting modes will now be compared with the literature, with consideration being given to the centered and wall-adjacent modes in that order.

For the centered case, the usable literature information is that of refs. [4, 5]. In both of those investigations the phase change medium was *n*-octadecane paraffin, and the melted mass was determined photographically as described earlier. In contrast, *n*-eicosane was the present phase change medium, and the melted mass was found by direct measurements.

It has been found that the effect of natural convection on the melting results can be taken into account by replacing *FoSte* with either $FoSteGr^m$ or $FoSteRa^n$, where *Gr* and *Ra* respectively represent the Grashof and Rayleigh numbers. In ref. [5], a correlation was achieved using the latter form with $n = 1/5$ and, in addition, *Ste* was replaced by $(Ste)^*$ to account for possible initial subcooling ΔT_{sub} of the solid below the melting temperature, where

$$(Ste)^* = Ste/(1 + S_c), \quad S_c = c_{sol}\Delta T_{sub}/\lambda. \quad (22)$$

In Fig. 6, the present M/M_{tot} data for the centered mode have been replotted using the $Fo(Ste)^*Ra^{1/5}$ abscissa variable suggested by ref. [5]. The slight initial subcooling used in the experiments yielded an S_c value of 0.00388. Furthermore, in deference to ref. [5], the liquid properties were evaluated at a temperature $(T_w + T^*)/2$. Inspection of the figure shows that the data (the open symbols) have been brought together in a tight band and the separate dependence on *Ste*, which was in evidence in Fig. 5, has been eliminated.

The solid line in Fig. 6 is a least-squares fit of the experimental data of ref. [5, equation (15)]. Also appearing in the figure are data (black symbols) from ref. [4], uncorrected since $S_c \ll 1$. The fact that the literature data lie below those of the present experiments is expected in light of the foregoing discussion of the photographic technique used in refs. [4, 5] for the determination of M. Another factor which contributes to the deviation is the accuracy of the measurement of the cross-sectional area of the solid from the photographs which, according to ref. [5], has a 5% uncertainty. Also, uncertainties in the thermo-

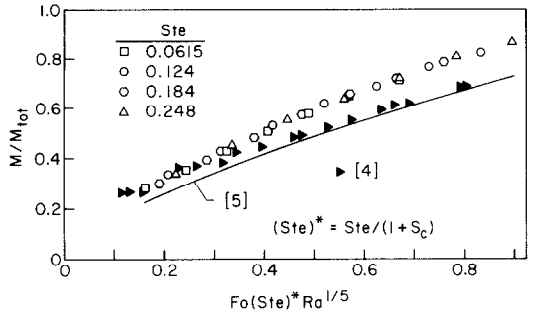

FIG. 6. Comparison of centered (i.e. constrained) melting results with the literature.

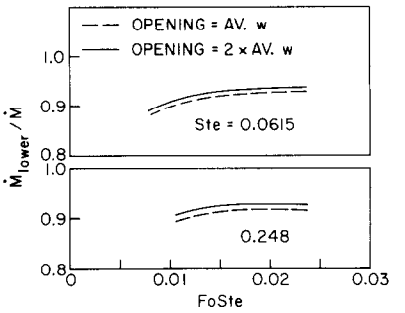

FIG. 8. Comparison of lower-surface rate of melting with overall rate of melting (wall-adjacent mode of melting).

physical properties of the participating liquids, *n*-eicosane and *n*-octadecane, may be another cause of the deviation in evidence in Fig. 6.

Attention is now turned to a comparison of the present results for the wall-adjacent mode with the literature. In ref. [7], a semi-predictive equation was derived for the timewise variation of the melted mass. In order to use this equation, the value of *FoSte* at which $M/M_{tot} = 1$ is needed. Here, by fairing a curve through the M/M_{tot} vs *FoSte* data, the required value of *FoSte* was found to be 0.0319. However, for design, where the $M/M_{tot} = 1$ value of *FoSte* is unknown, the equation cannot be used.

Figure 7 shows the present data (with properties evaluated at T^*) along with the aforementioned semi-predictive equation. Good agreement is seen to prevail at larger values of *FoSte*, but there is a difficult-to-rationalize tendency for deviations at lower *FoSte*. The data of ref. [7] appear to be well represented by the semi-predictive equation.

MELTED MASS DISTRIBUTION FOR WALL-ADJACENT MODE

As described earlier in the paper, the numerical solutions yielded the rate of melting $\dot{M}_{upper}$ at the upper surface of the solid for the wall-adjacent mode. In addition, values of the overall rate of melting $\dot{M}$ (at both surfaces) were obtained from the experimental data both by graphical and numerical techniques. From this information, the ratio $\dot{M}_{upper}/\dot{M}$ was formed at a succession of *FoSte* values for each of the four investigated *Ste*. Since it was thought to be of greater relevance, $\dot{M}_{lower}/\dot{M} = 1-(\dot{M}_{upper}/\dot{M})$ will be presented, where $\dot{M}_{lower}$ is the rate of melting at the lower surface.

In Fig. 8, $\dot{M}_{lower}/\dot{M}$ is plotted vs *FoSte* for the lowest and highest of the investigated *Ste* (the results for the intermediate *Ste* are available in ref. [9]). Results are shown for solutions based on the two adopted models of mass flow into the natural convection zone, namely: (a) an inflow opening equal to the average thickness w of the gap between the lower surface of the solid and the tube wall; and (b) an opening equal to twice the average thickness.

Inspection of the figure shows that the rate of melting at the lower surface is in the range 88–94% of the overall rate of melting. Thus, the conduction-based melting at the lower surface fully dominates the natural-convection-based melting at the upper surface. The aforementioned range is similar to the 85–90% suggested in ref. [7] on the basis of approximate experimental determinations. Further inspection of the figure shows that $\dot{M}_{lower}/\dot{M}$ is little affected by the model used for the mass inflow opening.

The distribution of the local Nusselt number [equation (20)] along the upper surface of the melting solid was also determined from the numerical solutions. A representative sample of the computed distributions, in the form of *Nu* vs θ, is displayed in Fig. 9, which corresponds to *Ste* = 0.124. An inset at the

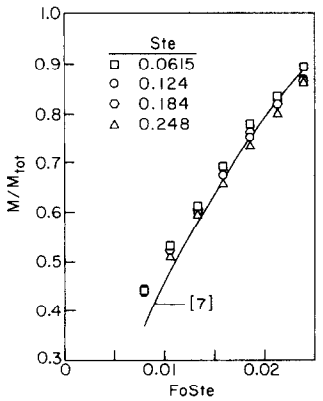

FIG. 7. Comparison of wall-adjacent (i.e. unconstrained) melting with the literature.

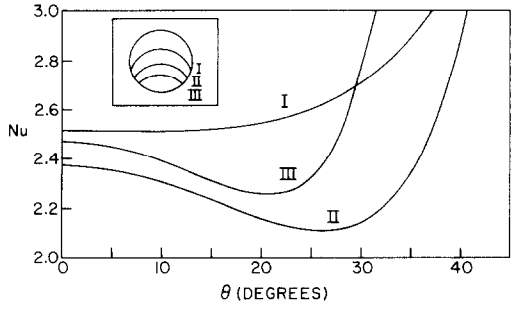

FIG. 9. Representative local Nusselt number distributions along the upper surface of the solid (wall-adjacent mode of melting).

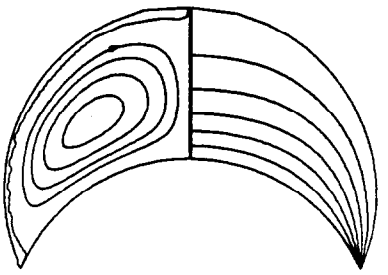

FIG. 10. Representative streamlines and isotherms (wall-adjacent mode of melting).

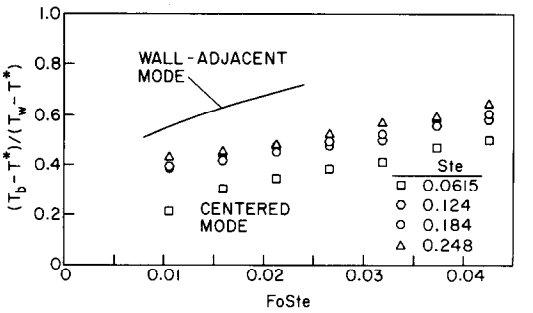

FIG. 11. Measured values of the liquid bulk temperature.

upper left of the figure shows the position of the upper surface for each of the selected cases designated as I, II and III, for which the *FoSte* values are 0.008, 0.016 and 0.024. The θ coordinate is illustrated in Fig. 1, with $\theta = 0°$ corresponding to the cross-section symmetry line AB.

The figure shows that with increasing angular distance from the symmetry line, *Nu* tends either to decrease or remain nearly constant. At still larger angular positions, the Nusselt number increases markedly. This increase can be attributed primarily to the growth of the heat conduction between the surface of the solid and the tube wall, a growth brought about by the decrease in the distance between the surface and the wall.

Representative streamlines and isotherms are presented in Fig. 10. The figure corresponds to *Ste* = 0.124 and to *FoSte* = 0.016 (i.e. case II of Fig. 9). Owing to symmetry, the streamlines need to be shown in only one half of the cross section and similarly for the isotherms. The streamlines display a recirculating flow of the type that is expected for natural convection. The wall-adjacent streamline is seen to be perturbed by the stepwise approximation of the tube wall, but the streamlines away from the wall are smooth. It may also be observed that the throughflow moves through the space along a wall-adjacent path and does not appear to mix with the recirculating flow. The isotherms pinch together in the inflow opening, indicating the presence of large temperature gradients and high heat transfer rates in that neighborhood.

ENERGY QUANTITIES

The energy input E_λ required to melt the mass M is available from Fig. 5, since, as noted earlier, $E_\lambda = \lambda M_{tot}(M/M_{tot})$. To evaluate the energy input E_s required for the increase in the sensible heat of the liquid melt, the liquid bulk temperature T_b is needed. The experimentally determined bulk temperatures are plotted in dimensionless form in Fig. 11 as a function of the *FoSte* dimensionless time. The data for the centered mode are plotted as such, while for the wall-adjacent mode, where the data are compact and show no consistent trend with *Ste*, a representative line is shown. Indeed, even for the centered mode, the data are insensitive to *Ste*, except for the lowest *Ste*. The separation of the latter data from the others is believed to be due to the less vigorous natural convection for that case.

For both modes of melting, the bulk temperature increases with time.The rate of increase is moderated by the continuous addition of new liquid at temperature T^* to the melt. The bulk temperatures for the wall-adjacent mode exceed those for the centered mode and the rate of increase is greater. This behavior may be attributed to the fact that for the former, most of the heating of the liquid occurs in the narrow gap adjacent to the lower surface of the solid. This heating is more efficient than that which occurs in the relatively large annular space which separates the solid and the tube wall in the centered mode.

The experimentally determined bulk temperatures for the wall-adjacent mode may be compared with those evaluated from the numerical solutions. However, a comparison with more physical content can be made in terms of E_s/E_λ. Such a comparison is displayed in Fig. 12, where E_s/E_λ is plotted as a function of *FoSte* for parametric values of *Ste*.

An overall inspection of the figure shows good agreement between the experimental and numerical results. For example, for *Ste* = 0.248, the maximum deviation is 7%. It is also seen that E_s/E_λ is larger at higher values of *Ste*, which is consistent with the interpretation of the Stefan number as a measure of the ratio of the sensible heat to the latent heat. As time proceeds during the melting period, E_s/E_λ increases for all Stefan numbers.

From the energy standpoint, the quantity of

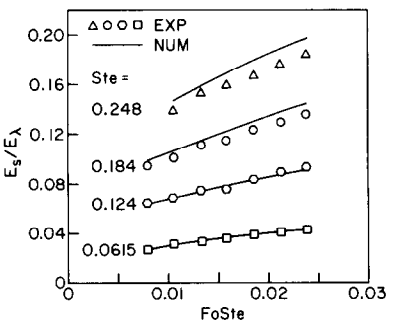

FIG. 12. Comparison of experimental and numerical results for E_s/E_λ (wall-adjacent mode of melting).

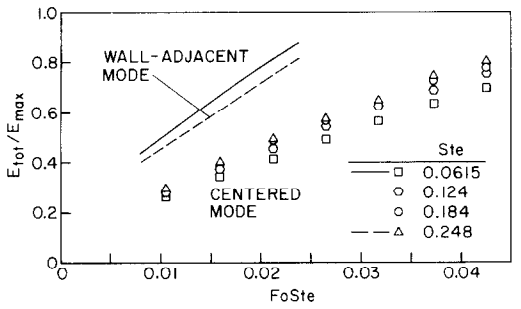

FIG. 13. Total (latent plus sensible) energy transferred in the wall-adjacent and centered modes of melting.

greatest practical relevance is the E_{tot}/E_{max} ratio, which measures the fraction of E_{max} that is transferred between $t = 0$ and $t = t$. The E_{tot}/E_{max} results are presented in Fig. 13 for both the wall-adjacent and centered modes. Overall, there is a strong resemblance between Fig. 13 and Fig. 5, which is as it should be since the latent heat contributions λM and λM_{tot} respectively dominate E_{tot} and E_{max}. Therefore, the trends that were identified in connection with Fig. 5 also pertain to Fig. 13.

The main practical message of Fig. 13 is the superiority of the wall-adjacent mode as a means for the rapid transfer of energy. For instance, whereas $E_{tot}/E_{max} \cong 0.5$ is achieved at $FoSte = 0.01$–0.0115 for the wall-adjacent mode, it is not achieved until $FoSte = 0.021$–0.027 for the centered mode. Therefore, if rapid energy transport is the objective of the design, it is appropriate to use the wall-adjacent mode rather than the centered mode.

CONCLUDING REMARKS

The work described here has provided a definitive comparison between melting in a horizontal tube in which the solid is either constrained to be stationary or may freely fall to the bottom of the tube due to gravity. At a given duration of the melting period, the amount of mass melted in the unconstrained mode exceeded that melted in the constrained mode by 50–100%, depending on the operating conditions. Similar gains occurred in the amount of energy transferred from the tube wall to the phase-change medium. Therefore, from the standpoint of the attainment of rapid energy transfer, the unconstrained mode of melting is clearly superior. Numerical solutions showed that about 90% of the melting in the unconstrained mode occurred at the lower portion of the solid, which is in very close proximity to the lower portion of the tube wall.

Photographic evidence was presented to demonstrate that the melting process in the contrained mode is intrinsically three-dimensional due to three-dimensional motions in the liquid melt. On the other hand, in the absence of end effects, the unconstrained-mode melting is two-dimensional.

REFERENCES

1. J. Pannu, G. Joglekar and P. A. Rice, Natural convection heat transfer to cylinders of phase change material used for thermal storage, *A.I.Ch.E. Symp. Ser.* **76**(198), 47–55 (1980).
2. K. Katayama, A. Saito, Y. Utaka, A. Saito, H. Matsui, H. Maekawa and A. Z. A. Saifulla, Heat transfer characteristics of the latent heat thermal storage capsule, *Sol. Energy* **27**, 91–97 (1981).
3. T. Saitoh and K. Hirose, High Rayleigh number solutions to problems of latent heat thermal energy storage in a horizontal cylinder capsule, *J. Heat Transfer* **104**, 545–553 (1982).
4. H. Rieger, U. Projahn, M. Bareiss and H. Beer, Heat transfer during melting inside a horizontal tube, *J. Heat Transfer* **105**, 226–234 (1983).
5. C. J. Ho and R. Viskanta, Heat transfer during inward melting in a horizontal tube, *Int. J. Heat Mass Transfer* **27**, 705–716 (1984).
6. D. Nicholas and Y. Bayazitoglu, Heat transfer and melting front within a horizontal cylinder, *J. sol. Energy Engng* **102**, 229–232 (1980).
7. M. Bareiss and H. Beer, An analytical solution of the heat transfer process during melting of an unfixed solid phase change material inside a horizontal tube, *Int. J. Heat Mass Transfer* **27**, 739–746 (1984).
8. E. I. Griggs and W. R. Humphries, A design handbook for phase change thermal control and energy storage devices, NASA Technical Paper 1074 (1977).
9. G. T. Geiger, Melting of an encapsulated solid, either fixed or free to fall under gravity, with or without rotation. Ph.D. thesis, Department of Mechanical Engineering, University of Minnesota, Minneapolis, MN (1985).
10. S. V. Patankar, *Numerical Heat Transfer and Fluid Flow*. Hemisphere, Washington, DC (1980).
11. A. Settari and K. Aziz, A generalization of the additive–correction methods for the iterative solution of matrix equations, *SIAM J. Numer. Anal.* **10**, 506–521 (1973).
12. R. E. Powe, C. T. Carley and E. H. Bishop, Free convective flow patterns in cylindrical annuli, *J. Heat Transfer* **91**, 310–314 (1969).
13. U. Grigull and W. Hauf, Natural convection in horizontal cylindrical annuli, *Proc. Third Int. Heat Transfer Conference*, Vol. 2, pp. 182–195 (1966).
14. J. Lis, Experimental investigation of natural convection heat transfer in simple and obstructed horizontal annuli, *Proc. Third Int. Heat Transfer Conference*, Vol. 2, pp. 196–204 (1966).
15. Y. F. Rao, Y. Miki, K. Fukuda, Y. Takata and S. Hasegawa, Flow patterns of natural convection in horizontal cylindrical annuli, *Int. J. Heat Mass Transfer* **28**, 705–714 (1985).
16. H. T. Rossby, A study of Bénard convection with and without rotation, *J. Fluid Mech.* **36**, 309–335 (1969).
17. S. H. Davis, U. Müller and C. Dietsche, Pattern selection in single-component systems coupling Bénard convection and solidification, *J. Fluid Mech.* **144**, 133–151 (1984).

FUSION DANS UN TUBE HORIZONTAL AVEC LE SOLIDE LIBRE OU NON DE TOMBER PAR GRAVITATION

Résumé—Des expériences et des solutions numériques supplémentaires sont conduites pour étudier la fusion d'un solide encapsulé dans un tube horizontal. Dans une série d'expériences, le solide ne peut pas se déplacer tandis que dans une seconde le solide peut tomber librement en gravitation. Dans ce dernier cas la portion inférieure du solide est séparée du tube par un mince film liquide. Les solutions numériques permettent de déterminer la vitesse de fusion dans les portions basse et haute du solide libre. A une période donnée de la fusion, la quantité de masse fondue dépasse ce qui serait fondu dans le cas non libre de 50 à 100 pour cent, avec un gain semblable dans le transfert d'énergie. Pour le mode libre, environ 90 pour cent de la fusion se produit à la partie basse du solide. Une observation photographique montre que le mécanisme de fusion non libre est intrinséquement tridimensionnel, tandis qu'en l'absence des effets de bout la fusion libre est bidimensionnelle.

SCHMELZEN IN EINEM HORIZONTALEN ROHR MIT FESTGEHALTENER ODER FREIER FESTER PHASE

Zusammenfassung—Versuche und ergänzende numerische Berechnungen wurden über den Schmelzvorgang eines Mediums in einem waagerechten Rohr durchgeführt. In der ersten Versuchsreihe wurde die feste Phase festgehalten, in einer zweiten konnte sie sich unter dem Einfluß der Schwerkraft frei bewegen. Im letzteren Fall wurde der untere Teil der festen Phase durch einen engen, flüssigkeitsgefüllten Spalt von der Rohrwand getrennt. Mit Hilfe der numerischen Lösung konnte das Schmelzverhalten oben und unten an der frei beweglichen festen Phase bestimmt werden. Nach einer bestimmten Schmelzzeit war im Fall der frei beweglichen festen Phase 50% bis 100% mehr Material geschmolzen als bei festgehaltener fester Phase, entsprechend mehr Wärme wurde übertragen. Im frei beweglichen Fall schmolz 90% des Materials an der unteren Hälfte der festen Phase. Fotografien zeigen, daß der Schmelzprozeß im festgehaltenen Fall dreidimensional, im frei beweglichen Fall bei genügend langem Rohr zweidimensional ist.

ПЛАВЛЕНИЕ НАХОДЯЩЕГОСЯ В ГОРИЗОНТАЛЬНОЙ ТРУБЕ ТВЕРДОГО ТЕЛА В РЕЖИМАХ ЗАКРЕПЛЕНИЯ И СВОБОДНОГО ПАДЕНИЯ

Аннотация—Выполнены эксперименты и численные расчеты по изучению плавления твердого тела, заключенного в горизонтальную трубу. В одних экспериментах твердое тело закреплялось неподвижно внутри трубы, в других оно могло свободно перемещаться под действием силы тяжести. В последнем случае нижняя часть твердого тела была отделена от стенки трубы тонким слоем жидкости. Численные расчеты позволили определить скорости плавления в верхней и нижней областях незакрепленного твердого тела. При заданной длительности периода плавления количество расплавившейся массы в незакрепленном образце превосходило соответствующее количество в закрепленном на 50–100%, аналогично различался и энергоперенос. В незакрепленном режиме около 90% расплавившейся массы находилось в нижней части твердого тела. Полученные фотографии свидетельствуют, что при закреплении твердого тела процесс плавления является существенно трехмерным, в то время как в режиме свободного падения, если пренебречь краевыми эффектами, он имеет двумерных характер.